




The Pathogenic Sphingolipid Psychosine is Secreted in Extracellular Vesicles in the Brain of a Mouse Model of Krabbe Disease

ASN Neuro
Volume 14: 1–17
© The Author(s) 2022
Article reuse guidelines:
sagepub.com/journals-permissions
DOI: 10.1177/17590914221087817
journals.sagepub.com/home/asn


Cory R. Reiter¹ , Rima Rebiai¹, Angelika Kwak¹, Jeff Marshall¹, Dylan Wozniak¹, Giuseppe Scesa¹, Duc Nguyen¹, Emily Rue², Chandimal Pathmasiri³, Robert Pijewski⁴, Richard van Breemen², Stephanie Cologna³, Stephen J. Crocker⁴, M Irene Givogri¹ and Ernesto R Bongarzone¹ 

Abstract

Psychosine exerts most of its toxic effects by altering membrane dynamics with increased shedding of extracellular vesicles (EVs). In this study, we discovered that a fraction of psychosine produced in the brain of the Twitcher mouse, a model for Krabbe disease, is associated with secreted EVs. We evaluated the effects of attenuating EV secretion in the Twitcher brain by depleting ceramide production with an inhibitor of neutral sphingomyelinase 2, GW4869. Twitcher mice treated with GW4869 had decreased overall EV levels, reduced EV-associated psychosine and unexpectedly, correlated with increased disease severity. Notably, characterization of well-established, neuroanatomic hallmarks of disease pathology, such as demyelination and inflammatory gliosis, remained essentially unaltered in the brains of GW4869-treated Twitcher mice compared to vehicle-treated Twitcher controls. Further analysis of Twitcher brain pathophysiology is required to understand the mechanism behind early-onset disease severity in GW4869-treated mice. The results herein demonstrate that some pathogenic lipids like psychosine may be secreted using EV pathways. Our results highlight the relevance of this secretory mechanism as a possible contributor to spreading pathogenic lipids in neurological lipidoses.

Keywords

extracellular vesicles, exosomes, psychosine, lysosomes, demyelination, neurotoxicity

Received November 27, 2021; Revised February 26, 2022; Accepted for publication February 28, 2022

Introduction

Krabbe disease is a genetic leukodystrophy caused by mutations in the *GALC* gene, which encodes the lysosomal enzyme galactosylceramidase (GALC) (Krabbe, 1916; Suzuki and Suzuki, 1970, 1971; Zlotogora et al., 1990). GALC deficiency blocks the catabolism of galactosylceramides (GalCer) and leads to the toxic accumulation of the lysosphingolipid galactosylsphingosine or psychosine. Endogenous levels of psychosine are low in healthy conditions but its toxic accumulation correlates with disease progression and development of CNS and PNS pathology in Krabbe patients (Suzuki, 1998). Psychosine is primarily synthesized via deacylation of GalCer by acid ceramidase (Li et al., 2019) and is considered the molecular trigger in this disease (Miyatake and Suzuki, 1972). Twitcher mice represent an authentic model of infantile forms of Krabbe disease with diffuse central and peripheral demyelination,

microgliosis, astrogliosis and progressive neurodegeneration (Austin, 1962; Wallace et al., 1964; Kobayashi et al., 1980;

¹Department of Anatomy and Cell Biology, College of Medicine, University of Illinois at Chicago, Chicago, IL, USA

²Department of Pharmaceutical Science, College of Pharmacy, Oregon State University, Corvallis, OR, USA

³Department of Chemistry, College of Liberal Arts and Sciences, University of Illinois at Chicago, Chicago, IL, USA

⁴Department of Neuroscience, University of Connecticut Health Center, Farmington, CT, USA

Corresponding Authors:

Cory R. Reiter, Department of Anatomy and Cell Biology, College of Medicine, University of Illinois at Chicago, Chicago, IL, USA.
Email: creite3@uic.edu

Ernesto R. Bongarzone, Department of Anatomy and Cell Biology, College of Medicine, University of Illinois at Chicago, Chicago, IL, USA.
Email: ebongarz@uic.edu



Castelvetri et al., 2011; Cantuti-Castelvetri et al., 2012; Cantuti Castelvetri et al., 2013; Claycomb et al., 2014; Smith et al., 2014; Abdelkarim et al., 2018; Marshall et al., 2018).

How psychosine triggers pathogenic mechanisms has remained incompletely understood. Our laboratory discovered that psychosine accumulates in membrane lipid rafts, disrupting their architecture (White et al., 2009; White et al., 2011). It is believed that raft dysfunction plays a major role in modifying downstream signaling pathways such as IGF-receptor (Sural-Fehr et al., 2019), Akt (Cantuti-Castelvetri et al., 2015; Sural-Fehr et al., 2019), PKC (White et al., 2009; White et al., 2011; Hawkins-Salsbury et al., 2013) and phosphatases (Castelvetri et al., 2011; Cantuti-Castelvetri et al., 2012; Cantuti Castelvetri et al., 2013). Psychosine introduces steric hindrance impacting on lateral mobility and fluidity of cellular and myelin membranes (D'Auria and Bongarzone, 2016; Batta et al., 2018). In fact, we recently demonstrated that psychosine decreases membrane fluidity and facilitates the shedding and secretion of extracellular vesicles (EVs) (D'Auria et al., 2017). These findings and early imaging evidence of vesiculation of brain membranes in Twitcher mice, led us to question whether psychosine associates with secreted EVs.

EVs are highly heterogenous secreted membrane vesicles, participating in inter-cellular communication and propagation of signals (Trams et al., 1981; Johnstone et al., 1987; Colombo et al., 2014; Tricarico et al., 2017; Mathieu et al., 2019). The lipid composition of EVs is influenced by cell type, differentiation stage, age, metabolic status, and by disease state (Colombo et al., 2014; Willms et al., 2016; Reiter and Bongarzone, 2019; Willis et al., 2020). Once vesicles are formed, their targeting mechanism for cargo delivery is still uncertain. The lipid layer that protects the transported cargo facilitates mobilization over significant distances while evading degradative processes (They et al., 2006; Street et al., 2012; van Niel et al., 2018). These aspects are relevant when considering the implications for the propagation of pathogenic molecules such as psychosine. For example, EVs can carry pathogenic proteins such as amyloid and alpha-synuclein, likely contributing to seed formation of plaques in Alzheimer disease models and other proteopathic models (Danzer et al., 2012; Shi et al., 2014; Minakaki et al., 2018). While most studies of lipids involved in EV biology have characterized compositional changes contributing to EV formation (Skotland et al., 2017), little has been done to study whether EVs can also transport pathogenic lipids in genetic lipidoses. Here we have addressed this question in EVs of the Twitcher mouse brain.

Methods

Animals and Treatment Protocol

All procedures involving animals were conducted in accordance with protocols approved by the Animal Care and Use Committee

(Protocol Number 15–101). WT (GALC^{+/+}) and TWI (GALC^{-/-}) mice were maintained in a C57BL/6J background and genotype determined as described (Sakai et al., 1996). Animals were randomly distributed to treatment groups until the cohorts were complete as pre-determined by power analysis. Both male and female mice were utilized in this study, with sufficient mice per sex within each treatment group to allow for stratification of collected data by sex. Treatment groups consisted of WT and TWI mice subjected to pharmacologic inhibition of neutral sphingomyelinase 2 (nSMase2) by GW4869 (Cayman Chemical, RRDI: 13127) (2.5mg/kg) or DMSO vehicle only controls, starting at postnatal day 10 (P10) with separate groups for designated early (P20) and late (P40) stage disease collection end points. At collection time, mice were anesthetized with isoflurane, and transcardially perfused with PBS. Brain was removed, further processed for either biochemistry or histology as outlined below.

Animal Behavior and Disease Score

Before injections of GW4869 or DMSO diluted in saline, mice were assessed for disease scoring metrics as outlined in (Marshall et al., 2018). Grip strength was also assessed by recording the latency to fall from a wire hang challenge. Mice were placed on a mesh wire grid which was then positioned perpendicular to and approximately 30 cm above the home cage floor. The time mice remained on the grid was recorded, with a maximum time allotment of 45 s.

Peripheral Nerve Conduction Velocity

P30 animals (n = 4/group) were anesthetized and monitored for regular breathing and pain reactivity during myoelectrosurgery to expose the sciatic nerve. Electromyogram recordings were collected by inserting a 5-lead ECG/EEG/EMG cable into the gastrocnemius muscle and stimulating the sciatic nerve with dual gold needle electrodes. Action potentials were collected on an iWorx 228S Recorder (iWorx, Dover, NH) and analyzed using Matlab software based on our previous publication Dolcetta et al. (2005).

Isolation of Extracellular Vesicles from Brain Tissue

Following PBS perfusion, mouse brains were separated into left and right hemispheres; one half was weighed and snap frozen on dry ice and stored at -80°C until processing for extracellular vesicle isolation as previously described with minor modifications (Perez-Gonzalez et al., 2012). Techniques to isolate EV populations from tissues have been optimized to prevent cellular lysis and capture vesicles within the extracellular milieu (Dinkins et al., 2016; Vella et al., 2017). Each half-brain was thawed in a 60×15 mm petri dish and submerged in 1.5ml of cold digestion buffer and diced with a sterile scalpel. Digestion buffer was made fresh for each reaction comprised of 200 $\mu\text{g}/\text{mL}$ Cysteine (Sigma, RRDI: C7352-25G), 200 $\mu\text{g}/\text{mL}$ EDTA (Fisher

Scientific, RRDI: 60-00-4), 20 units/mL papain (Worthington, RRDI: LS003126) in HBSS without Calcium and Magnesium (Gibco, RRDI: 14175-095) and passed through a 0.22 μm filter (Millipore, RRDI: SLGP033RS). Following filtration, 1,000 units/mL DNase (Worthington, Cat #: LS002007) were added and the solution was adjusted to pH 7.4. The chopped brain in digestion buffer was then collected and incubated at 37°C for 15 min. A 25 μL aliquot of this completed digestion product was saved as a total homogenate (TH) sample and stored at -20°C . The remaining homogenate was passed through a 40 μm mesh filter (Corning, RRDI: 352340) and rinsed with 5 ml of PBS without Calcium and Magnesium (Corning, RRDI: 21-040-CV). The digested brain filtrate is subjected to multiple centrifugation steps, all completed at 4°C with the resultant pellets saved and stored at -20°C . The first spin at 300 \times g for 10 min produces a pellet (P1), and supernatant is then spun at 2,000 \times g for 10 min leading to the second pellet (P2). Supernatant from this spin is transferred to polyallomer ultracentrifuge tubes (Beckman-Coulter, RRDI: 331372) without filtration, a significant adaptation from the original method (Perez-Gonzalez et al., 2012). The volume is increased and balanced with PBS without Calcium and Magnesium prior to ultracentrifugation at 10,000 \times g for 30 min in an SW41 rotor on a Beckman-Coulter Optima XL-100 K ultracentrifuge. The resultant pellet (P3) is saved, and supernatant is moved to new ultracentrifuge tubes and spun at 100,000 \times g for 90 min to pellet extracellular vesicles. The resulting supernatant is discarded, and the pellet is resuspended in 2 mL of 0.95 M sucrose solution in PBS without Calcium and Magnesium. A sucrose step-gradient is made by layering six 2 mL steps into an ultracentrifuge tube starting from 2 M sucrose at the bottom up to 0.25 M sucrose in 0.35 M increments, with the 0.95 M step containing the resuspended EV pellet, as described. Tubes are balanced carefully with the 0.25 M sucrose and the gradient is spun at 200,000 \times g for 16 h. The sucrose gradient is collected by first removing the top 1 mL (fraction 1), followed by 4 \times 2 mL collections (fractions 2-5) to capture the interphase of each sucrose step, and the final 3 mL (fraction 6) without disturbing any products pelleted at the bottom of the tube. These fractions are placed in ultracentrifuge tubes and brought up to 12 mL with PBS without Calcium and Magnesium. Diluted fractions are then spun at 100,000 \times g for 90 min. Supernatant is discarded and EV pellets are resuspended in 100 μL of PBS without Calcium or Magnesium. Protein content was measured by BCA assay (Pierce, RRDI: 23225). EVs were stored at -20°C until further analysis. Isolation and storage conditions of the EVs followed established best practices as set forth by MISEV2018 (Thery et al., 2018).

Nanoparticle Tracking Analysis

Purified EVs were analyzed on a NanoSight NS300 instrument equipped with a 488 nm laser (Malvern Instruments, United

Kingdom) available in the flow cytometry core at UIC. Collection methods were optimized following parameters set forth by Gardiner et al (Gardiner et al., 2013). Briefly, appropriate dilution of each sample required empirical methods to obtain sensitivity and specificity of the particle tracking with approximately 100–200 particles/frame and greater than 200 tracks observed per sample. EV samples were diluted (1:25) in PBS without Calcium and Magnesium (Corning, RRDI: 21-040-CV) and injected using a motorized syringe pump speed of 100. Video recordings of 60 s repeated 5 times were collected for each sample, with consistent collection parameters of 30 frames per second, camera level 16, slider shutter 1300, and slider gain 512. Data were analyzed by NTA 3.2 software (Malvern Instruments) and distribution data were binned into sizes by 10nm in GraphPad Prism 8. Samples followed consistent dilutions, with some exceptions if data collection integrity was too low and an individualized dilution was required. Dilution parameters from brain-derived EVs were as follows: fraction 1, 1:100; fraction 2, 1:800; fraction 3, 1:800; fraction 4, 1:800; fraction 5, 1:200; fraction 6, 1:200.

Immunofluorescence

Following perfusion and extraction, half-brains were post-fixed in 4% paraformaldehyde for 12–24 h and transferred to PBS before being cryosectioned (30 μm) using a microtome and stored in cryoprotectant at -20°C until further processing. Select brain sections were removed and washed briefly in TBS before the free-floating sections were incubated in blocking buffer (0.3 M glycine, 1% BSA, 5% normal donkey serum, 0.3% Triton X-100 in TBS) for 1 h at room temperature. Primary antibody solutions were made in blocking buffer and incubated at 4°C for 48–72 h. Following TBS washes, free-floating sections were incubated in secondary antibody solutions diluted in blocking buffer for 2 h at room temperature. Final washes with PBS preceded tissue mounting on glass slides and mounting with Prolong Gold antifade reagent containing DAPI (Life Technologies, RRDI: P36931). Primary antibodies used included the following: GFAP (1:500, Millipore, RRDI: MAB3402), Iba1 (1:300, Wako Pure Chemical Industries, RRDI: 019-19741) and MBP (1:500). Secondary antibodies were all used at a dilution of 1:500 in blocking buffer, including anti-rabbit 488 (AlexaFluor 488, ThermoFisher, RRDI: A11034), and anti-mouse 549 (DyLight 549, ThermoFisher, RRDI: 715-506-020). The lipophilic dye Fluoromyelin Green (ThermoFisher, RRDI: F34651) was added into the secondary antibody solutions containing 0.3% Triton \times 100 at a 1:300 dilution and followed the same incubation parameters.

Immunofluorescent microscopy was performed on 2 different microscopes; composite images were collected on a Zeiss Imager M1 with motorized stage, while confocal images were collected using a Leica TCS SPE confocal laser with an upright DM5500Q Microscope (Leica

Biosystems, Buffalo Grove, IL). Images were analyzed for fluorescence intensity measurements after adjustments were made in ImageJ. All image files were collected using the same parameters and followed the same post-hoc manipulations. Regions of interest were drawn, and the raw integrated density values (summation of pixel intensities) were normalized to the square area of the region. Background subtraction of a relevant region was then used to render the final values reported. Immunofluorescence measurements were taken from 2 slices per animal with cohort analysis from $n = 3-4$ animals per treatment group, genotype and timepoint.

Immunoblotting

Tissues were homogenized in PBS without Calcium or Magnesium using a Vibra-cell ultrasonic liquid processor (model VCX 130, Sonics and Materials, Newton, CT) and quantified for protein (BCA). EV isolates were not further processed prior to gel loading. Samples were prepared with 20 μg of protein in LDS Sample Buffer containing 50mM DTT and boiled at 90°C for 5 min. Protein lysates and/or EV samples were loaded into a 1.5 mm 4%-12% Bis-Tris Protein Gel (ThermoFisher Scientific, RRDI: 1620177) and run at 120 Volts for approximately 2 h. Following electrophoresis, proteins were transferred onto polyvinylidene fluoride (PVDF) membrane (Bio-Rad, RRDI: 1620177) using a gel transfer box run at 0.35 Amps for 2 h with solution mixing. Membranes were blocked with 5% milk in TBS containing 0.1% Tween (TBS-T) for 1 h at room temperature. Primary antibodies were diluted in blocking solution and incubated at 4°C overnight. Primary antibodies and dilutions include anti-Rab5b (1:1,000, rabbit polyclonal IgG, Santa Cruz, RRDI: sc-598), anti-Alix (1:1,000, mouse monoclonal IgG1 κ , Millipore, RRDI: MABS1277), anti-PLP (1:2,000, a kind gift from Dr Robert Skoff, Detroit) and anti-GFAP (1:500, Millipore, RRDI: MAB3402). Following 3 \times 5 min washes with TBS-T, secondary antibodies were diluted in blocking solution and incubated at room temperature for 1 h. Secondary antibodies and dilutions used include 1:2,000 anti-rabbit and 1:5,000 anti-mouse antibodies, both conjugated to horse radish peroxidase (Cell Signaling, RRDI: 7074S & 7076S, respectively). Blots were developed using ECL reagent (ThermoFisher Scientific, RRDI: 32106) and imaged on an Odyssey Fc Imaging System (Licor Biosciences).

Transmission Electron Microscopy

EV preparations were fixed with 1% paraformaldehyde/1.25% glutaraldehyde in 0.1 M cacodylate buffer (pH 7.4) at 4°C. TEM processing and imaging was performed at the University of Connecticut.

Psychosine and Ceramide Analysis by Mass Spectrometry

Fresh frozen tissues ($n = 3-6$ mice per group) were homogenized in H₂O at 10 μL per mg of tissue weight, with a minimum of 200 μL using a Vibra-cell ultrasonic liquid processor (model VCX 130, Sonics and Materials, Newton, CT). Protein quantification was performed on tissue homogenates to normalize the sample inputs prior to lipid extraction. Psychosine was extracted and measured using liquid chromatography with tandem mass spectrometry (LC-MS/MS) using our previously described method (Marshall et al., 2018). Ceramide was analyzed after organic extraction via a MTBE lipid extraction method (Matyash et al., 2008) from 200 μg of protein equivalent of whole brain lysate. Cer(d18:1/17:0) commercial standard was used as the internal standard and Cer-d7-(d18:1/17:0) deuterated commercial standard was used to make the calibration curve for exact quantification. Lipid separation was performed using an Agilent 1290 Infinity II UHPLC system outfitted with an Agilent Poroshell 120 EC-C18 column (2.1 \times 100 mm, 2.7 μm). The column was maintained at 50 °C and operated at a flow rate of 0.25 mL/min. Mobile phases consisted of solvent (A) 90:10 (v/v) water:methanol with 0.05 mM ammonium fluoride and 10 mM ammonium acetate while solvent (B) 20:30:50 (v/v) acetonitrile:methanol:isopropanol with 0.05 mM ammonium fluoride and 10 mM ammonium acetate. From each sample, 4 μg protein equivalent was injected and analyzed in technical duplicates. Data acquisition was performed using an Agilent 6545 quadrupole time-of-flight mass spectrometer in positive ion mode m/z range 200–1700. A pooled sample was analyzed in positive ion polarity using iterative MS/MS with fixed collision energy of 25 eV. Iterative MS/MS data were searched in Lipid Annotator software (Agilent Technologies) for lipid identification. Peak areas of extracted ion chromatograms for ceramide lipids were obtained using Agilent MassHunter software.

Matrix-Assisted Laser Desorption/Ionization–Time of Flight (MALDI-TOF) Imaging

Fresh frozen brain tissues ($n = 3-6$ mice per group) were sectioned at -20°C using a Microm HM 525 cryostat (Thermo Fisher Scientific). Serial tissue sections of 10 μm thickness were thaw-mounted directly onto stainless steel MALDI plates and stored in -80°C . Prior to analysis, the plate was dried under vacuum for two minutes to remove residual moisture. The plate was then submerged in cold 50 mM ammonium formate for 20 s, the dried again. Matrix application was done using a home-built sublimation apparatus. Here, 1,5-Diaminonaphthalene (DAN) was sublimed on the MALDI plate to obtain the matrix density (0.18–0.22 mg/cm²). Mass spectrometry imaging was performed using a model 4800 Plus MALDI-TOF/TOF Analyzer (Sciex) equipped with a 200 Hz Nd-YAG (355 nm) pulsed laser.

Data were acquired in the negative ion reflectron mode. The number of laser shots per pixel was set to 50 and the raster distance between each pixel was set to 100 μm using the 4800 Imaging Tool v. 3.2 (<https://ms-imaging.org/wp/4000-series-imaging>). The acquired data were processed using MSiReader where MS images were normalized by their total ion current (TIC) (Alexandrov, 2012). Lipid assignments were made by comparing accurate mass measurements to the LIPID MAPS database.

Statistics

Power analyses were conducted using GPower 3.1 open-source software. Graphs were completed and statistics performed using Prism 8 software (GraphPad, La Jolla, CA). Collected data were analyzed using a Student t-test or two-way ANOVA with either Bonferroni or Tukey's post hoc analysis as appropriate. Graphs are shown as the mean of independent measurements and the standard error of the mean (SEM).

Results

Psychosine and Myelin Components in EVs Secreted in the Twitcher Brain

To determine whether psychosine uses the EV secretory pathway, we first optimized the isolation of EVs from brain tissue. For this, EV populations were isolated using buoyant density ultracentrifugation on a sucrose gradient. The method has been optimized as described (Pituch et al., 2015; Vella et al., 2017). The EVs were separated into subpopulations collected as fractions 1 through 6, from lowest to highest density, to allow further delineation of heterogeneous vesicle populations by density migration. These fractions demonstrated enrichment of canonical vesicle markers ALIX (Iavello et al., 2016) and Rab5b (Kim et al., 2012) (Figure 1A, box) in TWI and WT brain-derived EV fractions. The enrichment of both markers in TWI EVs is likely consequence of the accelerated shedding process that characterizes this mutant (D'Auria et al., 2017). The quantity of EVs within each fraction was determined using nanoparticle tracking analysis, which showed that the bulk of EVs were contained in fractions 2–4 (Figure 1A). An increase of the total number of EVs isolated from TWI brains at either P20 or P40 was measured (Figure 1B), although not reaching statistical significance when corrected by tissue weight. A significant decrease in the total number of EVs isolated from TWI and WT P40 brains was measured with respect to P20 brains (Figure 1B). The quality of total EV preparations isolated from WT and TWI P40 brain was controlled using TEM. Figures 1C and 1D show that both WT (Figure 1C) and TWI (Figure 1D) EVs display the stereotypic vesicular profile, while the quantitative TEM stratification of EVs by

size shows non-significant differences in abundance between genotypes in samples prepared for TEM (Figure 1E).

Next, we used tandem mass spectrometry (LC-MS/MS) to determine the extent to which psychosine was present in TWI EVs and whether there was any change in content during disease progression. LC-MS/MS analyses of fractions clearly showed significant increases of psychosine in TWI EVs, particularly in fractions 2, 3 and 4 (Figure 2A). The total content of psychosine in EVs represented about 13.8% and 11.8% of the total content of psychosine in the brain of P20 and P40 TWI mice, respectively. The total content of psychosine in TWI EVs does not differ significantly at each time point. However, the content of psychosine per EV when normalized per EV number and brain weight shows that EVs isolated from P40 TWI brains contain significantly higher levels of psychosine (Figure 2B). This increase in psychosine-associated with EVs paralleled the expected accumulation of this lipid in the brain of mutant mice during the demyelinating stage of the disease in the TWI mouse brain (White et al., 2009). This was also accompanied by increased levels of other myelin components in EVs isolated from P40 TWI brains, including myelin proteolipids (Figure 2C) and myelin basic proteins (MBPs) (not shown). To our knowledge, this is the first evidence that psychosine, the sphingolipid believed to trigger most of neuropathology in Krabbe disease, is released in EVs in the TWI brain.

Inhibition of Sphingomyelinase by GW4869 Reduced EVs in the Twitcher Brain

Asymmetric lipid composition in the inner and outer leaflets of the lipid bilayer highly influences areas of increased curvature and hence impact on the formation of EVs. For example, ceramides, locally produced at the plasma membrane by the hydrolysis of sphingomyelin via neutral sphingomyelinase 2, contribute to microdomain formation for vesicle budding (Trajkovic et al., 2008). Reducing ceramide production either genetically (Aubin et al., 2005) or chemically with the pharmacologic inhibitor GW4869 (Trajkovic et al., 2008; Menck et al., 2017) significantly decreases cellular release of EVs. GW4869 is a neutral, non-competitive inhibitor of sphingomyelinase which blocks the budding in multivesicular bodies (Essandoh et al., 2015) and has been successfully used to reduce the secretion of EVs in vivo (Dinkins et al., 2014). We hypothesized that the reduction of EV release would negatively impact on the homeostasis of EV-associated psychosine, and on disease progression. To test this, TWI and WT control mice were treated with intraperitoneal injections of GW4869 during their peak of myelination and until reaching terminal stages of disease.

Our treatment protocol successfully decreased ceramide levels in the brain of P40 TWI mice who received the inhibitor compared to DMSO only vehicle. Figure 3A and 3B show decreased levels of Ceramide 32:2 and 36:2 across the TWI brain, as determined using mass spectrometry imaging by

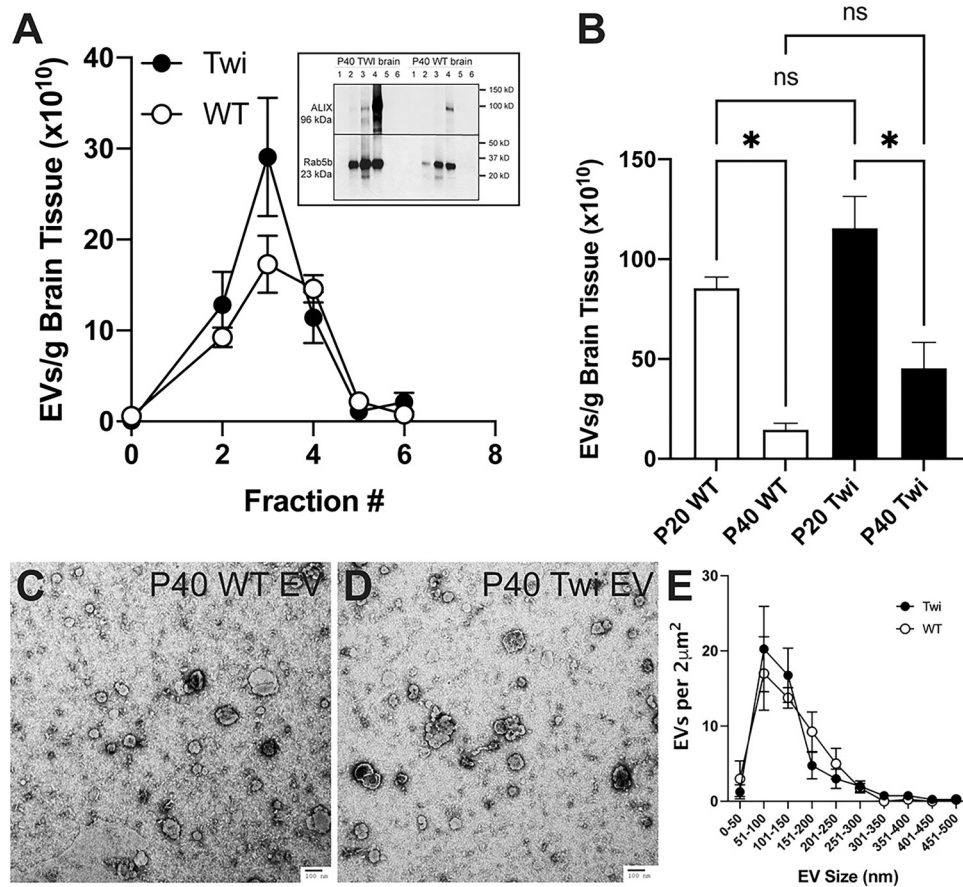


Figure 1. Isolation of extracellular vesicles from the brain. A) Extracellular vesicles (EVs) were isolated from the brain of wild-type (WT) and Twitcher (TWI) postnatal day (P) P40 as described in the methods section. Six fractions were obtained and the number of EVs in each fraction quantitated by NTA analysis as described. Box: fraction lysates were immunoblotted for ALIX and Rab5b. B) EVs were isolated from P20 and P40 brains, analyzed by NTA tracking, and fractions 2–5 quantitated and normalized by gram of tissue. ns, non-significant. C, D) EVs from P40 brains were processed, imaged (C) by TEM, and quantified as number of EV per $2\mu\text{m}^2$, and binned by size (D).

MALDI-TOF. LC-MS/MS analysis determination of total levels of ceramides confirmed this observation with significant decrease at P40 (Figure 3D, $p < 0.0001$) but not at P20.

The quantities of vesicles isolated from the brain tissues of treated TWI mice showed a significant decrease in total EVs at early stage (Figure 4A, $p = 0.0494$) but this trend was not significant at P40; however, specific fractions of EVs from GW4869-treated brains did show significant decreases compared to vehicle treated controls. In early-stage disease (Figure 4B), TWI mice treated with GW4869 had significantly reduced quantities of EVs in fractions 2 ($p = 0.0351$), 3 ($p = 0.0059$), and 4 ($p = 0.0003$). By P40 (Figure 4C), only fraction 3 ($p = 0.0012$) showed a significant decrease of EVs in GW4869-treated TWI brains. Analysis of vesicle size distribution (binned per 5nm diameter increments) showed that treatment with GW4869 inhibitor led to overall reduction of EVs in each fraction, without major shifts in EV size overall (Figure 4D shows an example of EV distribution in samples from P40 brains). In all, these data indicate that the GW469 inhibitor treatment was sufficient to reduce

total brain ceramide and in turn reduce the release of EVs in TWI brain during disease.

Analysis of psychosine in total brain homogenates showed no significant difference between GW4869-treated or vehicle treated TWI brain tissues at both early and late-stage disease (Figure 4E). Furthermore, there was no significant differences in the cumulative psychosine content of total EVs isolated from brain (Figure 4F), however, there were reductions of psychosine content associated with specific EV fractions. There were significantly reduced percentages of total psychosine in the isolates from GW4869-treated TWI brains relative to vehicle treated TWI brains in fractions 2 ($p = 0.0004$) and 3 ($p = 0.0038$) at P20 (Figure 4G), and fraction 3 ($p = 0.0002$) alone at P40 (Figure 4H). However, when the psychosine content is normalized to the number of EVs within each of the fractions, the relative quantity of psychosine per EV remains unchanged by the treatment at both P20 (not shown) and P40 (Figure 4I). This suggests that the reduction of psychosine is relative to the reduction of EVs within the EV fractions isolated from the brain tissues of

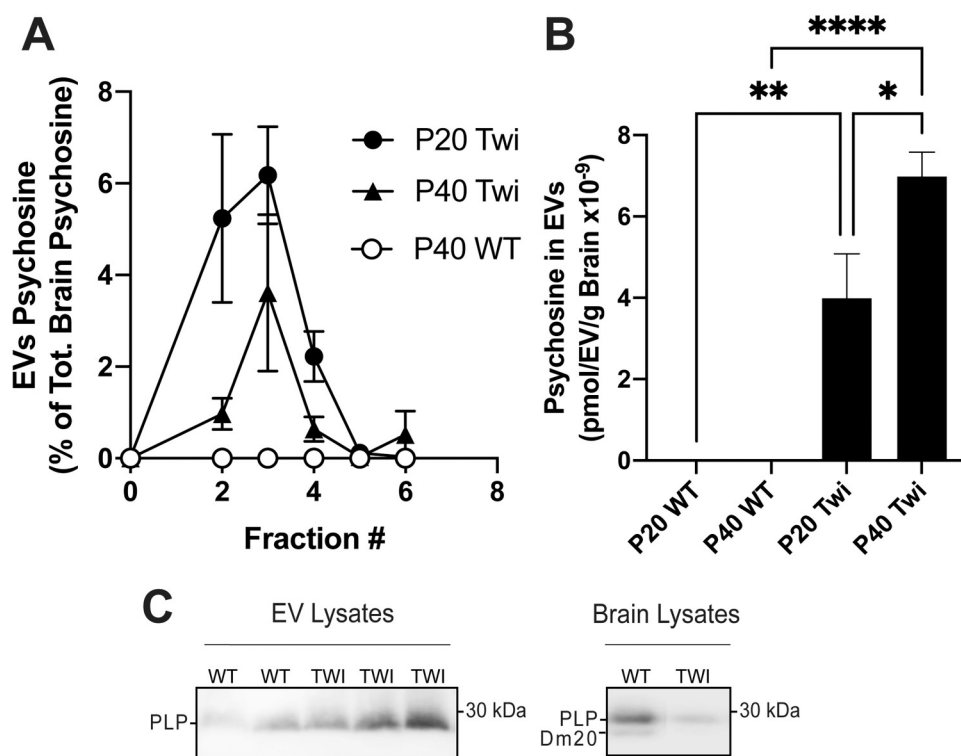


Figure 2. Psychosine measurement and detection of myelin proteins in extracellular vesicles from the twitcher brain. A,B) Extracellular vesicles (EVs) were isolated from the brain of wild-type (WT) and Twitcher (TWI) postnatal day (P) 20 and 40. Fractions 1–6 were processed for psychosine measurement by LC-MS-MS. Data are expressed as percent of the total brain psychosine (A) or normalized per number of EVs and weight (in grams) of brain tissue (B). C) EV protein extracts (10 μ g/lane) from two WT and three TWI P40 brains (left panel) were immunoblotted for myelin proteolipids. Right panel shows immunoblotting for myelin proteolipids of P40 WT and TWI total brain lysates (5 μ g/lane).

the inhibitor treated mice, but not a reduction of psychosine associated with the EVs of each fraction. Thus, the GW4869 paradigm seemed successful to decrease EVs in the TWI brain without altering psychosine production or its association with EVs.

Twitcher Mice Treated with GW4869 Reached Disease Stages Faster

We assessed the effect of GW4869 on disease severity and progression in TWI mice using our standardized disease severity scoring paradigm including ataxic gait, tremor, weight changes and latency to fall from a wire hang challenge. We found that while TWI mice treated with GW4869 reached the same levels of severity as vehicle-treated TWI mice during late stages of disease, treatment with GW4869 increased severity from P26-P30 (Figure 5A, $p=0.0017$, $p=0.0004$, $p<0.0001$, respectively) relative to vehicle-treated TWI mice. WT mice treated with vehicle or GW4869 showed no significant changes. The increased progression of disease signs in the GW4869-treated TWI mice was attributable to an earlier onset of ataxic gait (Figure 5B, $p<0.0001$) and the pathognomonic tremor (Figure 5C, $p=0.0099$), while

weight loss (Figure 5D) and wire hang challenge (Figure 5E) remained relatively unchanged. Conduction velocity studies on the sciatic nerve of P30 mice demonstrated reduced conduction velocities in TWI nerves compared to their WT counterparts, though treatment with GW4869 had no demonstrable effect (Figure 5F). These data show that depletion of EV populations in TWI mice is concomitant with an accelerated loss of some central neurological functions and an earlier acquisition of neurological signs, but without affecting the final stages of disease.

Gliosis Remained Unchanged After Treatment with GW4869

Krabbe disease histopathology has marked gliosis that intensifies with disease progression. Reactive astrocytes express glial fibrillary acidic protein (GFAP), denoting the level of astrogliosis in sagittal brain sections of TWI mice (Figure 6B). Although GW4869 treatment showed increases of GFAP positive astroglia (Figure 6A), these changes did not reach statistical significance (Figure 6D). A similar situation was observed with microglia. Expression of allograft inhibitory factor (Iba1) was used to quantify reactive

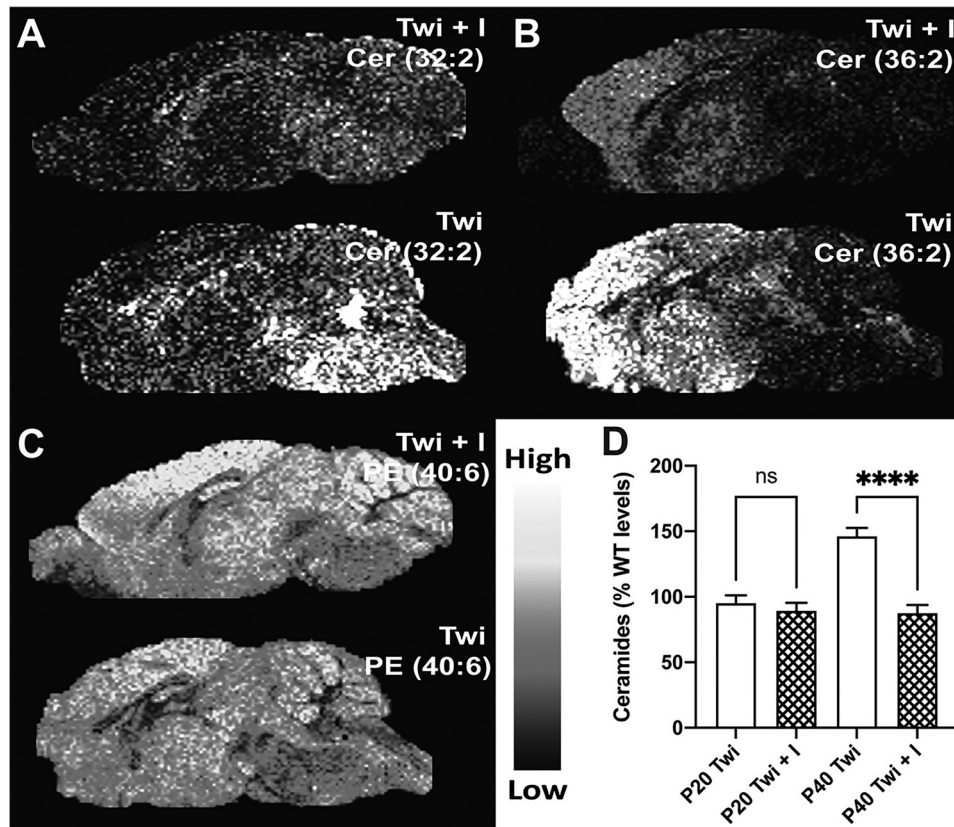


Figure 3. MALDI-TOF imaging of brain ceramides after treatment with GW4869. A-C) MALDI-TOF imaging of Ceramide (Cer) 32:2 (A), Cer 36:2 and phosphatidylethanolamine (PE) 40:6 in cryosections of P40 wild-type (WT) and Twitcher (TWI) brains after treatment with inhibitor (I) GW4869. D) Mass spectrometry quantification of total ceramides in P20 and P40 brains with and without treatment with GW4869.

microglia from brain slices of treated animals (Figure 6F). While TWI brains have overtly increased microgliosis (Figure 6F) in comparison to WT brains (Figure 6G), treatment with GW4869 also exhibited increases in Iba1 microgliosis (Figure 6E) which did not reach statistical significance (Figure 6H). These findings show that gliosis and inflammation remain at high levels in TWI mice treated with GW4869 and suggest that the faster development of neurological disease observed in GW4869-treated TWI mice may only contribute to the worsening of an already highly gliotic brain.

Demyelination remains largely unchanged in the TWI brain after treatment with Gw4869, with signs of minor improvement in the corpus callosum. To evaluate the effect of GW4869 on the overall level of demyelination in the TWI brain, myelin was microscopically assessed using the lipophilic dye, fluoromyelin, and by immunohistochemistry for myelin basic proteins (MBP). Fluoromyelin staining seemed relatively unchanged in the brain of GW4869-treated TWI mice (Figure 7A-C). Quantification of fluoromyelin fluorescence determined non-significant changes in the overall level of demyelination across the TWI brain after GW4869 treatment. Fluorescence

intensity in white matter from striatum, corpus callosum, and cerebellum were measured and showed non-significant differences with untreated TWI brains (Figure 7D). Likewise, MBP staining, which is a well-established method to evaluate gross levels of myelination in the brain, showed marginal reductions in the brain of GW4869-treated TWI mice, particularly in cerebellar white matter, and more localized areas in the striatum and medulla (Figure 7E-G). Despite this, MBP immunofluorescence quantification in striatum, corpus callosum, and cerebellum of GW4869-treated TWI mice showed non-significant differences with that from untreated TWI (Figure 7D). Further western blotting analysis of myelin proteolipids (PLP and Dm20) confirmed that treatment with GW4869 did not cause major measurable changes in myelin proteolipids either in P20 or P40 TWI brains (Figure 7I). Likewise, astrogliosis was confirmed by western blotting, showing high levels in both untreated and treated brains at either age (Figure 7I).

Discussion

This is the first investigation to our knowledge that identifies psychosine as a lipid cargo secreted by EVs in the brain of an

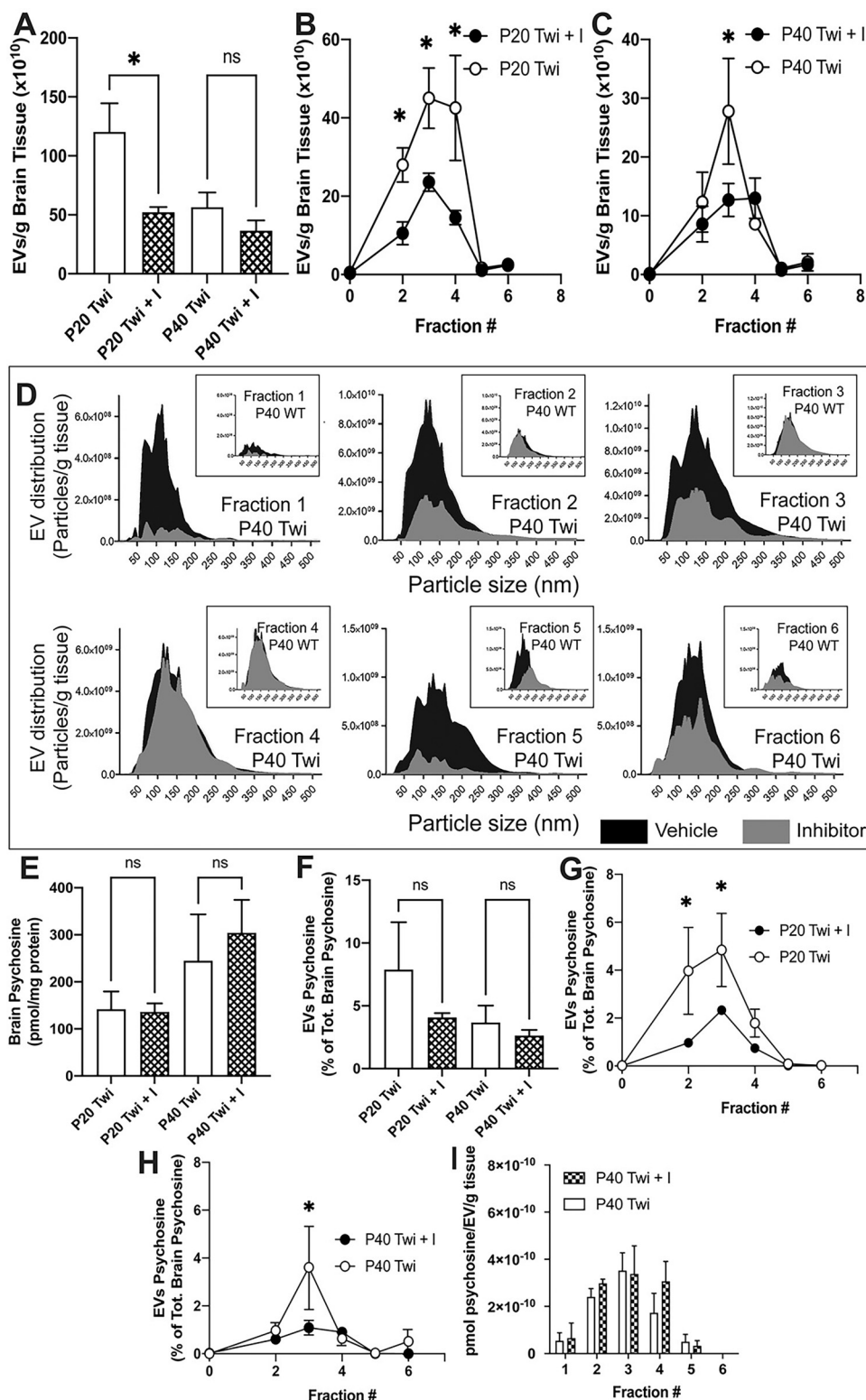


Figure 4. Effects on psychosine and EVs after treatment with GW4869. A-C) EVs were isolated from the brain of P20 and P40 wild-type (WT) and Twitcher (TWI) mice after treatment with inhibitor (I) GW4869 and analyzed by flow cytometry. Total numbers (A) and fractional numbers at P20 (B) and P40 (C) were determined. D) Effects of GW4869 on EV size are shown for each fraction of treated and untreated TWI EVs. Effects on size of WT EVs are depicted in the boxed graphs. E-H) Effects of GW4869 on total levels of psychosine in the brain (E), content of psychosine in total EVs (F) and in each EV fraction at P20 (G) and P40 (H) are shown. I) Normalization of psychosine concentration in EVs per wet weight of brain for each fraction is shown (I).

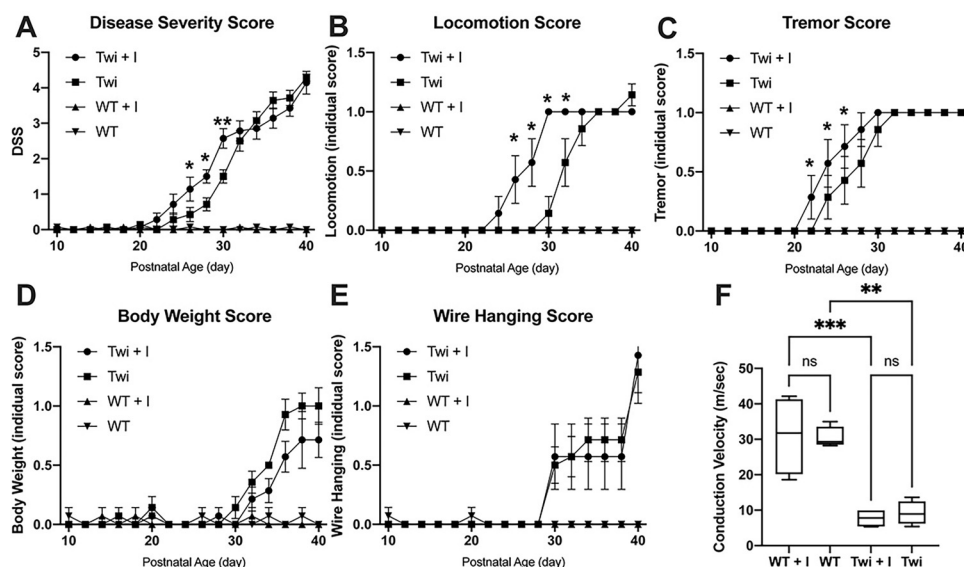


Figure 5. Disease severity scoring and peripheral conduction velocity after treatment with GW4869. A-E Twitcher (TWI) and wild-type (WT) mice were treated with GW4869 or vehicle as described in the methods section and the composite disease severity score (DSS) (A), locomotion score (B), tremor score (C), body weight score (D) and wire hanging score (E) were measured. F) Peripheral conduction velocity was measured in the sciatic nerve of P30 WT and TWI mice treated with GW4869 or with vehicle.

animal model of Krabbe disease. Our results show that a significant fraction of psychosine is present in total EVs isolated from the mutant brain, paralleling the development of disease. At early-stages, we found that TWI brains yielded greater numbers of EVs in fractions 2–4 as measured by NTA tracking. By late-stage disease EV quantities were reduced. Since this was consistent across both genotypes, this decrease is less likely to represent a pathologic process, but rather indicates that EV production and secretion are involved in normal neurodevelopmental physiology within the brain. The significance of this shift is difficult to interpret without further understanding the mechanisms that regulate EV release, which is beyond the scope of this study. EVs have been implicated in several neurodevelopmental and migratory processes within the central and peripheral nervous systems. Better understanding the course and fluctuations of EV release based on developmental processes is another interesting aspect to consider in future investigations of the CNS secretome.

Psychosine accumulation is inevitable in the Twitcher mouse model and Krabbe disease owing to catabolic enzyme insufficiency without redundant mechanisms for lipid breakdown. As such, psychosine degradative capacity within lysosomes and autophagosomes is limited, with toxic levels eventually leading to cell dysfunction and apoptosis. Accumulation of psychosine occurs in both neuronal and glial cell types, as well as in the myelin membranes themselves (D'Auria et al., 2017). Therefore, myelin sheaths act as another source of psychosine accretion, ultimately leading to their instability and degradation. EVs may serve as an mechanism for cells to escape or reduce toxic levels

of psychosine, though recipient cells would become likewise burdened. To better understand the role of EVs in psychosine accumulation and distribution within the Twitcher mouse model, we aimed to disrupt EV release with the pharmacologic inhibitor GW4869.

The number of EVs isolated from brains of mice treated with the GW4869 inhibitor of nSMase2 was reduced, with decreased quantities of EVs across multiple fractions of vesicle subpopulations. This reduction was more pronounced in early-stage disease but persisted into late-stage disease as well. We speculate that the diminished reduction of EVs in late-stage disease could be due to: 1) the efficacy of GW4869 to inhibit EV release requires a higher baseline level of EV release, therefore its inhibitory effect was decreased as EV release reduced with age in the TWI mice; 2) the mechanism of vesicle release in early disease has greater dependence on ceramide and diminishes with age; 3) the specific cell populations that contribute to secretion and/or clearance of EVs decrease EV-related functions over time.

Importantly, the total levels of psychosine within the brain and the psychosine content per EV remained unchanged by GW4869 treatment. The total content of psychosine released in EVs was only marginally reduced in summated EV populations following GW4869 treatment, but was significantly reduced in fractions 2 and 3 at P20, and in fraction 3 at P40. This suggests that the reduction of secreted psychosine in specific EV fractions is possibly due to an overall reduction of the secretion of EVs after GW4869 treatment, rather than a decreased association of psychosine with EVs. Importantly, our findings that a significant amount of psychosine was secreted regardless of GW4869 treatment suggest that

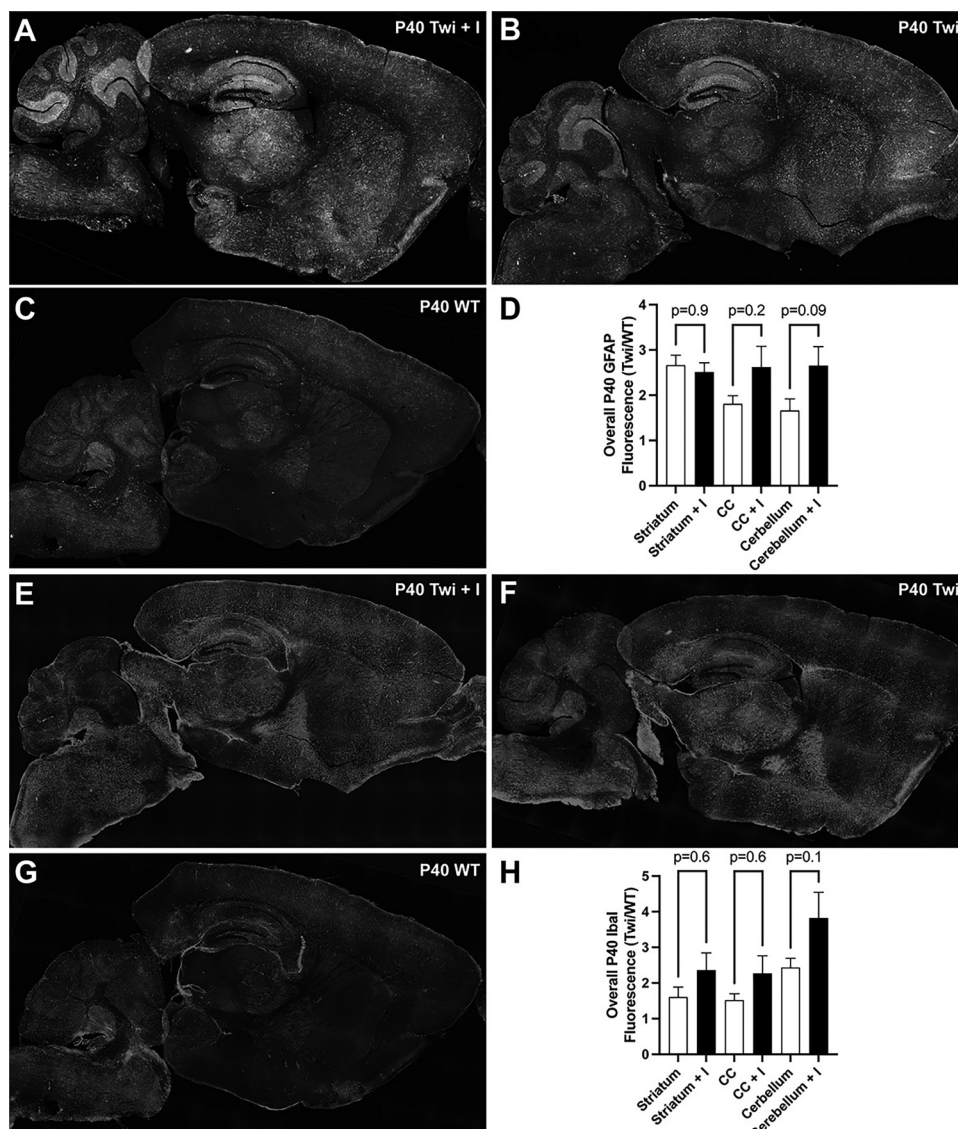


Figure 6. Gliosis in the brain of Twitcher mice after treatment with GW4869. A-D) Astroglia in the brain of P40 wild-type (WT) and Twitcher (TWI) mice after treatment with inhibitor (I) GW4869 was studied by immunohistochemical detection of GFAP (A-C). The relative fluorescence was quantified and plotted in (D). E-H) Microglia was studied by immunohistochemical detection of Iba-1 (E-G). The relative fluorescence was quantified and plotted in (H).

psychosine is released using additional secretory pathways (Bobrie et al., 2011).

Interestingly, the reduced secretion of psychosine in EVs in GW4869-treated mice paralleled an increased disease severity in treated TWI mice, primarily during the early phase of the disease. While the use of GW4869 successfully reduced pathology in other studies (Dinkins et al., 2014) there are also reports showing the opposite effect (Iguchi et al., 2016). An additional aspect to note is that EVs play an important role in cell-to-cell communication (Colombo et al., 2014; van Niel et al., 2018; Mathieu et al., 2019; Reiter and Bongarzone, 2019; Willis et al., 2020). Decreasing the secretion of EVs, as done in our study, may

have affected the transfer of relevant/key information possibly contributing to the worsened clinical phenotype in GW4869-treated Twitcher mice. While we have not observed signs of neurological disease in GW4869-treated WT mice, suggesting the absence of GW4869-related side effects, there are reports where some level of toxicity has been found following administration of GW4869 (Tabatadze et al., 2010; Essandoh et al., 2015; Tan et al., 2018). Thus, being that TWI mice are intrinsically vulnerable, potential GW4869-related toxicity may have also contributed to the worsening of treated TWI mice.

The apparent worsening of diffuse demyelination in TWI mice treated with GW4869 may explain the measurable

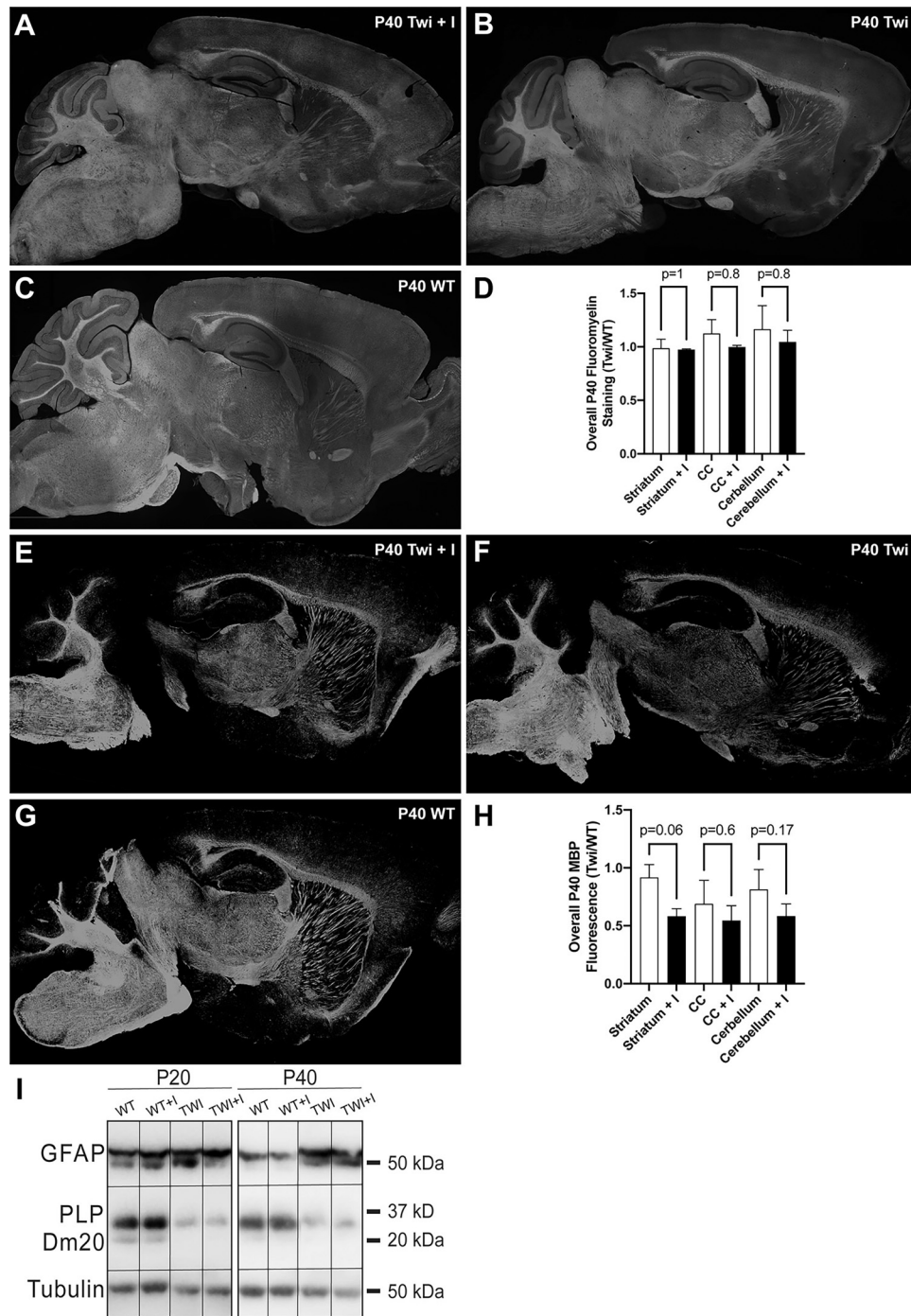


Figure 7. Myelin in the brain of Twitcher mice after treatment with GW4869. A-D) Myelin status in the brain of P40 wild-type (WT) and Twitcher (TWI) mice after treatment with inhibitor (I) GW4869 was studied by fluorescent detection of fluoromyelin (A-C). The relative fluorescence was quantified and plotted in (D). E-H) Myelin was also studied by immunohistochemical detection of MBP (E-G). The relative fluorescence was quantified and plotted in (H). I) Levels of GFAP and myelin proteolipids (PLP and Dm20) were studied by immunoblotting of total proteins extracted from P20 and P40 WT and TWI brains treated with vehicle or inhibitor (I) GW4869 as described in the methods. Tubulin was used as housekeeping protein.

increase of disease severity in these mice before reaching terminal neurological deterioration. One possibility is that in the naïve TWI brain, the secretion of psychosine in EVs aids to

reduce cellular levels of psychosine in myelinating cells such as oligodendrocytes, acting as a defense mechanism to decrease cellular stress. When this secretory pathway is

repressed with GW4869, TWI oligodendrocytes may have less opportunity to reduce their psychosine levels, eventually increasing cellular and myelin stress. In this context, our histological analyses showed regional reductions of MBP staining, suggesting loss or disruption of myelin membranes, albeit in non-significant levels with respect to the already demyelinated naïve TWI brain with an intact EV secretory pathway. The lack of power in detecting significant decreases of myelin after GW4869 treatment may also represent the contribution of the asynchronous pattern of differentiation and myelination of oligodendrocytes during the duration of our experiment, hence masking regional losses by the already highly demyelinating environment of the TWI brain.

Ceramide is a metabolite in the same synthetic pathway as psychosine, however its depletion did not cause changes in the total levels of psychosine within treated brain tissues. This is likely because *de novo* synthesis (Li et al., 2019) and alternative catabolic enzymes were not affected by GW4869 treatment. This pharmacologic inhibitor is specific to neutral sphingomyelinase 2, and as such should lead to ceramide depletion at specific subcellular sites without total reduction of ceramide lipid species (Dinkins et al., 2014; Essandoh et al., 2015; Menck et al., 2017). This was also demonstrated with MALDI-TOF analysis which showed region-specific reductions unique to different ceramide lipid species. Areas with notably decreased levels of ceramide included the corpus callosum and striatum. These areas, which are normally heavily myelinated, showed to have reduced myelin staining in the treated TWI brain, although not reaching significance when compared to the untreated TWI brain.

The GW4869 inhibitor used in this study likely impacts only a subpopulation of highly heterogeneous vesicles in the secretome. EVs have traditionally been classified based on their biogenesis, including the 3 main subgroups of exosomes, ectosomes and apoptotic bodies, though new mechanisms of EV release are continually being established (Tricarico et al., 2017; van Niel et al., 2018). The size ranges and biomarkers associated with each of these classifications often overlap, making the heterogeneity of EVs even more difficult to address when considering experimental design and data interpretation.

Research to characterize and understand the function of EVs has expanded greatly over the last decade, including the development of established nomenclature and methods to improve the generalizability and reproducibility of EV data. However, most studies have been conducted using cell culture systems or small sample cohorts from patient data owing to the technical difficulties of conducting rigorous *in vivo* analysis of EVs. Despite these challenges, the field has identified crucial roles of EVs in both normal homeostasis and pathogenesis of numerous disease states, including neurodegenerative disorders and cancer. EVs have been shown to contribute to normal brain physiology in cortical development through Shh signaling (Tanaka et al., 2005), synapse

maintenance (Lachenal et al., 2011), activity-dependent pruning (Paolicelli and Ferretti, 2017), and clearance of neuronal debris following trauma (Sokolowski et al., 2014). However, EVs have also been implicated in a number of traumatic or neurodegenerative diseases. Microglia have been shown to have increased EV release following TBI and leading to pro-inflammatory signaling in the secondary phase of injury (Kumar et al., 2017). Increased circulating EVs have been identified in the MS patients (Minagar et al., 2001), and have been suggested as a strong marker of neuroinflammation derived from patient CSF (Verderio et al., 2012). Just as in our study which identified propagation of a toxic lipid, EVs have also been implicated in the spread of misfolded protein aggregates such as tau in Alzheimer's disease (Iba et al., 2013; Aulston et al., 2019) and alpha-synuclein in Parkinson's disease (Alvarez-Erviti et al., 2011; Stuenkel et al., 2016). We are only just beginning to comprehend the propensity for EVs to serve as important molecular signaling mechanisms. The ability of EVs to transmit intracellular communication across long distances, evade immune detection, maintain relative stability, and cross stringent barriers make them lucrative candidates to improve our understanding of cell function in health and disease.

Acknowledgments

The study was supported with grants from the National Institutes of Health (R01 NS065808), Legacy of Angels Foundation, and the European Leukodystrophy Association to ERB. CRR was a fellow by the Chicago Consortium for Translational Science. The authors also acknowledge support from the UIC Department of Chemistry and College of Liberal Arts and Sciences (to SMC) as well as the UIC Graduate College (to KCP).

Declaration of Conflicting Interests


The author(s) declared the following potential conflicts of interest with respect to the research, authorship, and/or publication of this article: ERB is a consultant for Lysosomal Therapeutics Inc., E-Scape Bio, Gain Therapeutics, Neurogene Therapeutics, and Affinia Therapeutics. Neither entity provided support in the form of salaries for any listed author nor played additional roles in the design, data collection and analysis, decision to publish, or preparation of this manuscript.

Funding

The author(s) disclosed receipt of the following financial support for the research, authorship, and/or publication of this article: This work was supported by the Legacy of Angels Foundation, National Institute of Neurological Disorders and Stroke (grant number R01 NS065808), Association Européenne contre les Leucodystrophies.

ORCID iDs

Cory. R. Reiter  <https://orcid.org/0000-0003-0220-2127>

Ernesto. R. Bongarzone  <https://orcid.org/0000-0003-1664-6634>

References

- Abdelkarim, H., Marshall, M. S., Scesa, G., Smith, R. A., Rue, E., Marshall, J., Elackattu, V., Stoskute, M., Issa, Y., Santos, M., Nguyen, D., Hauck, Z., van Breemen, R., Celej, M. S., Gaponenko, V., & Bongarzone, E. R. (2018). alpha-Synuclein interacts directly but reversibly with psychosine: Implications for alpha-synucleinopathies. *Scientific Reports*, *8*, 12462. <https://doi.org/10.1038/s41598-018-30808-9>
- Alexandrov, T. (2012). MALDI Imaging mass spectrometry: Statistical data analysis and current computational challenges. *BMC Bioinformatics*, *13*(Suppl 16), S11–S11. <https://doi.org/10.1186/1471-2105-13-S16-S11>
- Alvarez-Erviti, L., Seow, Y., Yin, H., Betts, C., Lakhali, S., & Wood, M. J. (2011). Delivery of siRNA to the mouse brain by systemic injection of targeted exosomes. *Nature Biotechnology*, *29*, 341–345. <https://doi.org/10.1038/nbt.1807>
- Aubin, I., Adams, C. P., Opsahl, S., Septier, D., Bishop, C. E., Auge, N., Salvayre, R., Negre-Salvayre, A., Goldberg, M., Guenet, J. L., & Poirier, C. (2005). A deletion in the gene encoding sphingomyelin phosphodiesterase 3 (Smpd3) results in osteogenesis and dentinogenesis imperfecta in the mouse. *Nature Genetics*, *37*, 803–805. <https://doi.org/10.1038/ng1603>
- Aulston, B., Liu, Q., Mante, M., Florio, J., Rissman, R. A., & Yuan, S. H. (2019). Extracellular vesicles isolated from familial Alzheimer's disease neuronal cultures induce aberrant Tau phosphorylation in the wild-type mouse brain. *Journal of Alzheimer's Disease: JAD*, *72*, 575–585. <https://doi.org/10.3233/JAD-190656>
- Austin, J. (1962). Histochemical and biochemical studies in diffuse cerebral sclerosis (metachromatic and globoid-body forms). In p 35. Stuttgart, Thieme: Internation Congress on Neuropathology.
- Batta, G., Soltesz, L., Kovacs, T., Bozo, T., Meszar, Z., Kellermayer, M., Szollosi, J., & Nagy, P. (2018). Alterations in the properties of the cell membrane due to glycosphingolipid accumulation in a model of gaucher disease. *Scientific Reports*, *8*, 157. <https://doi.org/10.1038/s41598-017-18405-8>
- Bobrie, A., Colombo, M., Raposo, G., & Thery, C. (2011). Exosome secretion: Molecular mechanisms and roles in immune responses. *Traffic (Copenhagen, Denmark)*, *12*, 1659–1668. <https://doi.org/10.1111/j.1600-0854.2011.01225.x>
- Cantuti Castelvetti, L., Givogri, M. I., Hebert, A., Smith, B., Song, Y., Kaminska, A., Lopez-Rosas, A., Morfini, G., Pigino, G., Sands, M., Brady, S. T., & Bongarzone, E. R. (2013). The sphingolipid psychosine inhibits fast axonal transport in krabbe disease by activation of GSK3beta and deregulation of molecular motors. *Journal of Neuroscience*, *33*, 10048–10056. <https://doi.org/10.1523/JNEUROSCI.0217-13.2013>
- Cantuti-Castelvetti, L., Maravilla, E., Marshall, M., Tamayo, T., D'Auria, L., Monge, J., Jeffries, J., Sural-Fehr, T., Lopez-Rosas, A., Li, G., Garcia, K., van Breemen, R., Vite, C., Garcia, J., & Bongarzone, E. R. (2015). Mechanism of neuromuscular dysfunction in krabbe disease. *Journal of Neuroscience*, *35*, 1606–1616. <https://doi.org/10.1523/JNEUROSCI.2431-14.2015>
- Cantuti-Castelvetti, L., Zhu, H., Givogri, M. I., Chidavaenzi, R. L., Lopez-Rosas, A., & Bongarzone, E. R. (2012). Psychosine induces the dephosphorylation of neurofilaments by deregulation of PP1 and PP2A phosphatases. *Neurobiology of Disease*, *46*, 325–335. <https://doi.org/10.1016/j.nbd.2012.01.013>
- Castelvetti, L. C., Givogri, M. I., Zhu, H., Smith, B., Lopez-Rosas, A., Qiu, X., van Breemen, R., & Bongarzone, E. R. (2011). Axonopathy is a compounding factor in the pathogenesis of krabbe disease. *Acta Neuropathologica*, *122*, 35–48. <https://doi.org/10.1007/s00401-011-0814-2>
- Claycomb, K. I., Winokur, P. N., Johnson, K. M., Nicaise, A. M., Giampetruzzi, A. W., Sacino, A. V., Snyder, E. Y., Barbarese, E., Bongarzone, E. R., & Crocker, S. J. (2014). Aberrant production of tenascin-C in globoid cell leukodystrophy alters psychosine-induced microglial functions. *Journal of Neuropathology & Experimental Neurology*, *73*, 964–974. <https://doi.org/10.1097/NEN.0000000000000000117>
- Colombo, M., Raposo, G., & Thery, C. (2014). Biogenesis, secretion, and intercellular interactions of exosomes and other extracellular vesicles. *Annual Review of Cell and Developmental Biology*, *30*, 255–289. <https://doi.org/10.1146/annurev-cellbio-101512-122326>
- Danzer, K. M., Kranich, L. R., Ruf, W. P., Cagsal-Getkin, O., Winslow, A. R., Zhu, L., Vanderburg, C. R., & McLean, P. J. (2012). Exosomal cell-to-cell transmission of alpha synuclein oligomers. *Molecular Neurodegeneration*, *7*, 42. <https://doi.org/10.1186/1750-1326-7-42>
- D'Auria, L., & Bongarzone, E. R. (2016). Fluid levity of the cell: role of membrane lipid architecture in genetic sphingolipidoses. *Journal of Neuroscience Research*, *94*, 1019–1024. <https://doi.org/10.1002/jnr.23750>
- D'Auria, L., Reiter, C., Ward, E., Moyano, A. L., Marshall, M. S., Nguyen, D., Scesa, G., Hauck, Z., van Breemen, R., Givogri, M. I., & Bongarzone, E. R. (2017). Psychosine enhances the shedding of membrane microvesicles: implications in demyelination in Krabbe's disease. *PLoS One*, *12*, e0178103.
- Dinkins, M. B., Dasgupta, S., Wang, G., Zhu, G., & Bieberich, E. (2014). Exosome reduction in vivo is associated with lower amyloid plaque load in the 5XFAD mouse model of Alzheimer's disease. *Neurobiology of Aging*, *35*, 1792–1800. <https://doi.org/10.1016/j.neurobiolaging.2014.02.012>
- Dinkins, M. B., Enasko, J., Hernandez, C., Wang, G., Kong, J., Helwa, I., Liu, Y., Terry, A. V., & Bieberich, E. (2016). Neutral sphingomyelinase-2 deficiency ameliorates Alzheimer's disease pathology and improves cognition in the 5XFAD mouse. *The Journal of Neuroscience*, *36*, 8653–8667. <https://doi.org/10.1523/JNEUROSCI.1429-16.2016>
- Dolcetta, D., Amadio, S., Guerrini, U., Givogri, M. I., Perani, L., Galbiati, F., Sironi, L., Del Carro, U., Roncarolo, M. G., & Bongarzone, E. (2005). Myelin deterioration in twitcher mice: Motor evoked potentials and magnetic resonance imaging as in vivo monitoring tools. *Journal of Neuroscience Research*, *81*, 597–604. <https://doi.org/10.1002/jnr.20574>
- Essandoh, K., Yang, L., Wang, X., Huang, W., Qin, D., Hao, J., Wang, Y., Zingarelli, B., Peng, T., & Fan, G. C. (2015). Blockade of exosome generation with GW4869 dampens the sepsis-induced inflammation and cardiac dysfunction. *Biochimica et Biophysica Acta*, *1852*, 2362–2371. <https://doi.org/10.1016/j.bbadis.2015.08.010>
- Gardiner, C., Ferreira, Y. J., Dragovic, R. A., Redman, C. W., & Sargent, I. L. (2013). Extracellular vesicle sizing and enumeration by nanoparticle tracking analysis. *Journal of Extracellular Vesicles*, *2*. <https://doi.org/10.3402/jev.v2i0.19671>
- Hawkins-Salsbury, J. A., Parameswar, A. R., Jiang, X., Schlesinger, P. H., Bongarzone, E., Ory, D. S., Demchenko, A. V., & Sands, M. S. (2013). Psychosine, the cytotoxic sphingolipid that accumulates in globoid cell leukodystrophy, alters membrane

- architecture. *Journal of Lipid Research*, 54, 3303–3311. <https://doi.org/10.1194/jlr.M039610>
- Iavello, A., Frech, V. S., Gai, C., Deregiibus, M. C., Quesenberry, P. J., & Camussi, G. (2016). Role of alix in miRNA packaging during extracellular vesicle biogenesis. *International Journal of Molecular Medicine*, 37, 958–966. <https://doi.org/10.3892/ijmm.2016.2488>
- Iba, M., Guo, J. L., McBride, J. D., Zhang, B., Trojanowski, J. Q., & Lee, V. M. (2013). Synthetic tau fibrils mediate transmission of neurofibrillary tangles in a transgenic mouse model of Alzheimer's-like tauopathy. *Journal of Neuroscience*, 33, 1024–1037. <https://doi.org/10.1523/JNEUROSCI.2642-12.2013>
- Iguchi, Y., Eid, L., Parent, M., Soucy, G., Bareil, C., Riku, Y., Kawai, K., Takagi, S., Yoshida, M., Katsuno, M., Sobue, G., & Julien, J. P. (2016). Exosome secretion is a key pathway for clearance of pathological TDP-43. *Brain*, 139, 3187–3201. <https://doi.org/10.1093/brain/aww237>
- Johnstone, R. M., Adam, M., Hammond, J. R., Orr, L., & Turbide, C. (1987). Vesicle formation during reticulocyte maturation. Association of plasma membrane activities with released vesicles (exosomes). *Journal of Biological Chemistry*, 262, 9412–9420. [https://doi.org/10.1016/S0021-9258\(18\)48095-7](https://doi.org/10.1016/S0021-9258(18)48095-7)
- Kim, H. S., Choi, D. Y., Yun, S. J., Choi, S. M., Kang, J. W., Jung, J. W., Hwang, D., Kim, K. P., & Kim, D. W. (2012). Proteomic analysis of microvesicles derived from human mesenchymal stem cells. *Journal of Proteome Research*, 11, 839–849. <https://doi.org/10.1021/pr200682z>
- Kobayashi, T., Yamanaka, T., Jacobs, J. M., Teixeira, F., & Suzuki, K. (1980). The twitcher mouse: An enzymatically authentic model of human globoid cell leukodystrophy (krabbe disease). *Brain Research*, 202, 479–483. [https://doi.org/10.1016/0006-8993\(80\)90159-6](https://doi.org/10.1016/0006-8993(80)90159-6)
- Krabbe, K. H. (1916). A New familial, infantile form of diffuse brain-sclerosis. *Brain*, 39, 74–114. <https://doi.org/10.1093/brain/39.1-2.74>
- Kumar, A., Stoica, B. A., Loane, D. J., Yang, M., Abulwerdi, G., Khan, N., Kumar, A., Thom, S. R., & Faden, A. I. (2017). Microglial-derived microparticles mediate neuroinflammation after traumatic brain injury. *Journal of Neuroinflammation*, 14, 47. <https://doi.org/10.1186/s12974-017-0819-4>
- Lachenal, G., Pernet-Gallay, K., Chivet, M., Hemming, F. J., Belly, A., Bodon, G., Blot, B., Haase, G., Goldberg, Y., & Sadoul, R. (2011). Release of exosomes from differentiated neurons and its regulation by synaptic glutamatergic activity. *Molecular and Cellular Neurosciences*, 46, 409–418. <https://doi.org/10.1016/j.mcn.2010.11.004>
- Li, Y., Xu, Y., Benitez, B. A., Nagree, M. S., Dearborn, J. T., Jiang, X., Guzman, M. A., Woloszynek, J. C., Giaramita, A., Yip, B. K., Elsbernd, J., Babcock, M. C., Lo, M., Fowler, S. C., Wozniak, D. F., Vogler, C. A., Medin, J. A., Crawford, B. E., & Sands, M. S.,... (2019). Genetic ablation of acid ceramidase in krabbe disease confirms the psychosine hypothesis and identifies a new therapeutic target. *Proceedings of the National Academy of Sciences of the United States of America*, 116, 20097–20103. <https://doi.org/10.1073/pnas.1912108116>
- Marshall, M. S., Issa, Y., Jakubauskas, B., Stoskute, M., Elackattu, V., Marshall, J. N., Bogue, W., Nguyen, D., Hauck, Z., Rue, E., Karumuthil-Meethil, S., Zaric, V., Bosland, M., van Breemen, R. B., Givogri, M. I., Gray, S. J., Crocker, S. J., & Bongarzone, E. R. (2018). Long-Term improvement of neurological signs and metabolic dysfunction in a mouse model of krabbe's disease after global gene therapy. *Molecular Therapy*, 26, 874–889. <https://doi.org/10.1016/j.ymthe.2018.01.009>
- Mathieu, M., Martin-Jaular, L., Lavieu, G., & Thery, C. (2019). Specificities of secretion and uptake of exosomes and other extracellular vesicles for cell-to-cell communication. *Nature Cell Biology*, 21, 9–17. <https://doi.org/10.1038/s41556-018-0250-9>
- Matyash, V., Liebisch, G., Kurzchalia, T. V., Shevchenko, A., & Schwudke, D. (2008). Lipid extraction by methyl-tert-butyl ether for high-throughput lipidomics. *Journal of Lipid Research*, 49, 1137–1146. <https://doi.org/10.1194/jlr.D700041-JLR200>
- Menck, K., Sonmezer, C., Worst, T. S., Schulz, M., Dihazi, G. H., Streit, F., Erdmann, G., Kling, S., Boutros, M., Binder, C., & Gross, J. C. (2017). Neutral sphingomyelinases control extracellular vesicles budding from the plasma membrane. *Journal of Extracellular Vesicles*, 6, 1378056. <https://doi.org/10.1080/20013078.2017.1378056>
- Minagar, A., Jy, W., Jimenez, J. J., Sheremata, W. A., Mauro, L. M., Mao, W. W., Horstman, L. L., & Ahn, Y. S. (2001). Elevated plasma endothelial microparticles in multiple sclerosis. *Neurology*, 56, 1319–1324. <https://doi.org/10.1212/WNL.56.10.1319>
- Minakaki, G., et al. (2018). Autophagy inhibition promotes SNCA/alpha-synuclein release and transfer via extracellular vesicles with a hybrid autophagosome-exosome-like phenotype. *Autophagy*, 14, 98–119. <https://doi.org/10.1080/15548627.2017.1395992>
- Miyatake, T., & Suzuki, K. (1972). Globoid cell leukodystrophy: Additional deficiency of psychosine galactosidase. *Biochemical and Biophysical Research Communications*, 48, 539–543. [https://doi.org/10.1016/0006-291X\(72\)90381-6](https://doi.org/10.1016/0006-291X(72)90381-6)
- Paolicelli, R. C., & Ferretti, M. T. (2017). Function and dysfunction of microglia during brain development: consequences for synapses and neural circuits. *Frontiers in Synaptic Neuroscience*, 9, 9. <https://doi.org/10.3389/fnsyn.2017.00009>
- Perez-Gonzalez, R., Gauthier, S. A., Kumar, A., & Levy, E. (2012). The exosome secretory pathway transports amyloid precursor protein carboxyl-terminal fragments from the cell into the brain extracellular space. *Journal of Biological Chemistry*, 287, 43108–43115. <https://doi.org/10.1074/jbc.M112.404467>
- Pituch, K. C., Moyano, A. L., Lopez-Rosas, A., Marottoli, F. M., Li, G., Hu, C., van Breemen, R., Mansson, J. E., & Givogri, M. I. (2015). Dysfunction of platelet-derived growth factor receptor alpha (PDGFRalpha) represses the production of oligodendrocytes from arylsulfatase A-deficient multipotential neural precursor cells. *Journal of Biological Chemistry*, 290, 7040–7053. <https://doi.org/10.1074/jbc.M115.636498>
- Reiter, C. R., & Bongarzone, E. R. (2020). The role of vesicle trafficking and release in oligodendrocyte biology. *Neurochemical Research*, 45, 620–629.
- Sakai, N., Inui, K., Tatsumi, N., Fukushima, H., Nishigaki, T., Taniike, M., Nishimoto, J., Tsukamoto, H., Yanagihara, I., Ozono, K., & Okada, S. (1996). Molecular cloning and expression of cDNA for murine galactocerebrosidase and mutation analysis of the twitcher mouse, a model of krabbe's disease. *Journal of Neurochemistry*, 66, 1118–1124. <https://doi.org/10.1046/j.1471-4159.1996.66031118.x>
- Shi, M., Liu, C., Cook, T. J., Bullock, K. M., Zhao, Y., Ghingina, C., Li, Y., Aro, P., Dator, R., He, C., Hipp, M. J., Zabetian, C. P., Peskind, E. R., Hu, S. C., Quinn, J. F., Galasko, D. R., Banks, W. A., & Zhang, J. (2014). Plasma exosomal alpha-synuclein is likely CNS-derived

- and increased in Parkinson's disease. *Acta Neuropathologica*, 128, 639–650. <https://doi.org/10.1007/s00401-014-1314-y>
- Skotland, T., Sandvig, K., & Llorente, A. (2017). Lipids in exosomes: current knowledge and the way forward. *Progress in Lipid Research*, 66, 30–41. <https://doi.org/10.1016/j.plipres.2017.03.001>
- Smith, B. R., Santos, M. B., Marshall, M. S., Cantuti-Castelvetri, L., Lopez-Rosas, A., Li, G., van Breemen, R., Claycomb, K. I., Gallea, J. I., Celej, M. S., Crocker, S. J., Givogri, M. I., & Bongarzone, E. R. (2014). Neuronal inclusions of alpha-synuclein contribute to the pathogenesis of krabbe disease. *The Journal of Pathology*, 232, 509–521. <https://doi.org/10.1002/path.4328>
- Sokolowski, J. D., Chabanon-Hicks, C. N., Han, C. Z., Heffron, D. S., & Mandell, J. W. (2014). Fractalkine is a "find-me" signal released by neurons undergoing ethanol-induced apoptosis. *Frontiers in Cellular Neuroscience*, 8, 360. <https://doi.org/10.3389/fncel.2014.00360>
- Street, J. M., Barran, P. E., Mackay, C. L., Weidt, S., Balmforth, C., Walsh, T. S., Chalmers, R. T., Webb, D. J., & Dear, J. W. (2012). Identification and proteomic profiling of exosomes in human cerebrospinal fluid. *Journal of Translational Medicine*, 10, 5. <https://doi.org/10.1186/1479-5876-10-5>
- Stuendl, A., Kunadt, M., Kruse, N., Bartels, C., Moebius, W., Danzer, K. M., Mollenhauer, B., & Schneider, A. (2016). Induction of alpha-synuclein aggregate formation by CSF exosomes from patients with Parkinson's disease and dementia with Lewy bodies. *Brain*, 139, 481–494. <https://doi.org/10.1093/brain/awv346>
- Sural-Fehr, T., Singh, H., Cantuti-Catelvetri, L., Zhu, H., Marshall, M. S., Rebiai, R., Jastrzebski, M. J., Givogri, M. I., Rasenick, M. M., & Bongarzone, E. R. (2019). Inhibition of the IGF-1-PI3K-Akt-mTORC2 pathway in lipid rafts increases neuronal vulnerability in a genetic lysosomal glycosphingolipidosis. *Disease Models & Mechanisms*, 12.
- Suzuki, K. (1998). Twenty five years of the "psychosine hypothesis": A personal perspective of its history and present status. *Neurochemical Research*, 23, 251–259. <https://doi.org/10.1023/A:1022436928925>
- Suzuki, K., & Suzuki, Y. (1970). Globoid cell leucodystrophy (krabbe's disease): Deficiency of galactocerebroside beta-galactosidase. *Proceedings of the National Academy of Sciences of the United States of America*, 66, 302–309. <https://doi.org/10.1073/pnas.66.2.302>
- Suzuki, K., & Suzuki, Y. (1971). Krabbe's globoid cell leukodystrophy: Deficiency of galactocerebroside beta-galactosidase activity. *Journal of Neuropathology & Experimental Neurology*, 30, 145.
- Tabatadze, N., Savonenko, A., Song, H., Bandaru, V. V., Chu, M., & Haughey, N. J. (2010). Inhibition of neutral sphingomyelinase-2 perturbs brain sphingolipid balance and spatial memory in mice. *Journal of Neuroscience Research*, 88, 2940–2951.
- Tan, L. H., Tan, A. J., Ng, Y. Y., Chua, J. J., Chew, W. S., Muralidharan, S., Torta, F., Dutta, B., Sze, S. K., Herr, D. R., & Ong, W. Y. (2018). Enriched expression of neutral sphingomyelinase 2 in the Striatum is essential for regulation of lipid raft content and motor coordination. *Molecular Neurobiology*, 55, 5741–5756. <https://doi.org/10.1007/s12035-017-0784-z>
- Tanaka, Y., Okada, Y., & Hirokawa, N. (2005). FGF-induced vesicular release of sonic hedgehog and retinoic acid in leftward nodal flow is critical for left-right determination. *Nature*, 435, 172–177. <https://doi.org/10.1038/nature03494>
- Thery, C., et al. (2018). Minimal information for studies of extracellular vesicles 2018 (MISEV2018): A position statement of the international society for extracellular vesicles and update of the MISEV2014 guidelines. *Journal of Extracellular Vesicles*, 7, 1535750. <https://doi.org/10.1080/20013078.2018.1535750>
- Thery, C., Amigorena, S., Raposo, G., & Clayton, A. (2006). Isolation and characterization of exosomes from cell culture supernatants and biological fluids. *Curr Protoc Cell Biol Chapter*, 3, Unit 3 22.
- Trajkovic, K., Hsu, C., Chiantia, S., Rajendran, L., Wenzel, D., Wieland, F., Schwille, P., Brugger, B., & Simons, M. (2008). Ceramide triggers budding of exosome vesicles into multivesicular endosomes. *Science (New York, N.Y.)*, 319, 1244–1247. <https://doi.org/10.1126/science.1153124>
- Trams, E. G., Lauter, C. J., Salem, N Jr., & Heine, U. (1981). Exfoliation of membrane ecto-enzymes in the form of microvesicles. *Biochimica et Biophysica Acta*, 645, 63–70. [https://doi.org/10.1016/0005-2736\(81\)90512-5](https://doi.org/10.1016/0005-2736(81)90512-5)
- Tricarico, C., Clancy, J., & D'Souza-Schorey, C. (2017). Biology and biogenesis of shed microvesicles. *Small GTPases*, 8, 220–232. <https://doi.org/10.1080/21541248.2016.1215283>
- van Niel, G., D'Angelo, G., & Raposo, G. (2018). Shedding light on the cell biology of extracellular vesicles. *Nature Reviews Molecular Cell Biology*, 9, 213–228.
- Vella, L. J., Scicluna, B. J., Cheng, L., Bawden, E. G., Masters, C. L., Ang, C. S., Willamson, N., McLean, C., Barnham, K. J., & Hill, A. F. (2017). A rigorous method to enrich for exosomes from brain tissue. *Journal of Extracellular Vesicles*, 6, 1348885. <https://doi.org/10.1080/20013078.2017.1348885>
- Verderio, C., Muzio, L., Turola, E., Bergami, A., Novellino, L., Ruffini, F., Riganti, L., Corradini, I., Francolini, M., Garzetti, L., Maiorino, C., Servida, F., Vercelli, A., Rocca, M., Dalla Libera, D., Martinelli, V., Comi, G., Martino, G., & Matteoli, M.,... (2012). Myeloid microvesicles are a marker and therapeutic target for neuroinflammation. *Annals of Neurology*, 72, 610–624. <https://doi.org/10.1002/ana.23627>
- Wallace, B. J., Aronson, S. M., & Volk, B. W. (1964). Histochemical and biochemical studies of globoid cell Leucodystrophy (Krabbe's disease). *Journal of Neurochemistry*, 11, 367–376. <https://doi.org/10.1111/j.1471-4159.1964.tb11930.x>
- White, A. B., Galbiati, F., Givogri, M. I., Lopez Rosas, A., Qiu, X., van Breemen, R., & Bongarzone, E. R. (2011). Persistence of psychosine in brain lipid rafts is a limiting factor in the therapeutic recovery of a mouse model for Krabbe disease. *Journal of Neuroscience Research*, 89, 352–364. <https://doi.org/10.1002/jnr.22564>
- White, A. B., Givogri, M. I., Lopez-Rosas, A., Cao, H., van Breemen, R., Thinakaran, G., & Bongarzone, E. R. (2009). Psychosine accumulates in membrane microdomains in the brain of krabbe patients, disrupting the raft architecture. *Journal of Neuroscience*, 29, 6068–6077. <https://doi.org/10.1523/JNEUROSCI.5597-08.2009>
- Willis, C. M., Nicaise, A. M., Bongarzone, E. R., Givogri, M., Reiter, C. R., Heintz, O., Jellison, E. R., Sutter, P. A., TeHennepe, G., Ananda, G., Vella, A. T., & Crocker, S. J. (2020). Astrocyte support for oligodendrocyte differentiation can be conveyed via extracellular vesicles but diminishes with Age. *Scientific Reports*, 10, 828. <https://doi.org/10.1038/s41598-020-57663-x>
- Willms, E., Johansson, H. J., Mager, I., Lee, Y., Blomberg, K. E., Sadik, M., Alaarg, A., Smith, C. I., Lehtio, J., El Andaloussi,

S., Wood, M. J., & Vader, P. (2016). Cells release subpopulations of exosomes with distinct molecular and biological properties. *Scientific Reports*, *6*, 22519. <https://doi.org/10.1038/srep22519>

Zlotogora, J., Chakraborty, S., Knowlton, R. G., & Wenger, D. A. (1990). Krabbe disease locus mapped to chromosome 14 by genetic linkage. *American Journal of Human Genetics*, *47*, 37–44.